Simple Method for Calculating the Propagation of THz Radiation In Experimental Geometries

D. Côté, J.E. Sipe,* and H.M. van Driel

Department of Physics, University of Toronto, Toronto, Canada M5S 1A7

Abstract

A formalism based on plane wave decomposition is applied to the linear propagation of terahertz pulses in experimental geometries. The approach is very general and is not restricted to any particular polarization (or current) source. Near and far field expressions easily amenable to numerical computation are obtained for the temporal profiles and spectra of terahertz pulses in layered structures, as often encountered in experiments. The effects of polarization and angle-dependent multiple reflection and transmission, as well as material dispersion, are included. Examples for optical rectification in GaAs and ZnTe are presented to illustrate the simplicity of the method, and are compared with experiments. The numerical evaluation of the expressions for the THz electric field in practical experimental geometries is straightforward.

OCIS codes: 050.1940,320.7100,320.7120,350.5500,350.5610

*Electronic address: sipe@physics.utoronto.ca

1. Introduction

The temporal profile of an electromagnetic wave often carries important information about the source that generated it. A description of the effects of propagation on the temporal profile of such waves is often critical both in determining what information can be extracted from the measurements of the temporal profile and in extracting it. For experiments with simple boundary conditions[1], the properties of the radiation can be studied analytically. In more specialized applications, however, it is necessary to use approaches that allow some approximations to be made in order to extend the reach of analytical methods. In optics, for instance, one can use the paraxial wave equation to study the propagation of radiation in free space, and thereby derive important analytical expressions for the beam properties[2]. However, recent advances in the production of few-cycle ultrashort optical pulses[3], and THz pulses[4–6] have allowed the creation of electromagnetic pulses that cannot be described by the paraxial wave equation. These pulses are often used in situations where the phase of different frequency components with respect to the envelope function is critical. Experimental techniques have been developed to time-resolve the amplitude and phase of this radiation[4,7,8]. It has been shown that the respective time signatures of this radiation in the near field and far field are vastly different[9–11]. The full solution to Kirchoff's diffraction integral has been used to model some experiments and has yielded excellent agreement with experimental data[12]. Yet the generalization of this formalism to more complicated geometries, including interfaces, is not straightforward. And while solving Maxwell equations with finite-difference techniques is always an option, doing so can be difficult to implement, particularly in three dimensions[13].

The goal of this paper is to introduce a practical method for calculating radiated fields from any prescribed source, both in the near and far field, so that an easy comparison of

predicted results with experimental data can be achieved. This method permits the extraction of important details about the dynamics of the source that generated the radiation[14]. In this work, the propagation of broadband THz radiation in experimental situations is modelled taking into consideration polarization-dependent effects at interfaces, multiple reflections, dispersion of the index of refraction, as well as near and far field pulse reshaping effects. Sipe[15] has shown that a plane wave decomposition of the field allows the description of the propagation both in the near and far field in terms of simple, intuitive Green functions. The framework makes use of well-known results from linear optics (*e.g.*, complete frequency-dependent Fresnel transmission and reflection coefficients) and lends itself nicely to an analysis of relatively complex geometries with multiple reflections and arbitrary polarizations, as is the case in most practical studies.

The structure of this paper is as follows. In section 2, we build on earlier work[15] and introduce the formalism and notation. Next, in section 3, we describe the propagation of radiation through vacuum, dielectric media, and lenses. The results are then used in section 4 to obtain the Green functions for different geometries and calculate the radiation from an arbitrary polarization source. Finally, straightforward examples from realistic situations both in the near and far field are worked out, the results of which can be directly used in modelling most experimental situations.

2. Formalism

Plane waves and spherical waves are both eigenmodes of the Helmoltz equation. Therefore any propagating electromagnetic field can be expressed as a superposition of either plane or spherical waves. The key advantage in using plane waves over spherical waves is that the description of transmission and reflection at interfaces takes a simple form, in that the $\hat{s}$- and $\hat{p}$-polarized components of the field can usually be treated independently. Expressions for

the propagation through any layered media, using results from thin film optics, can then be easily obtained. For these reasons, we employ a plane wave basis with polarization vectors $\hat{s}$ and $\hat{p}$. Each plane wave is fully defined by four parameters: its frequency Ω, its wave vector $\boldsymbol{\nu}$, its polarization vector ($\hat{s}$ or $\hat{p}$) and, finally, its complex amplitude. The wave vector $\boldsymbol{\nu}$ is further decomposed into two components: $\pm w$ (possibly complex) along the axial direction $\hat{z}$, and $\boldsymbol{K}$ (always real) in the xy plane transverse to $\hat{z}$. The vector $\boldsymbol{R} = R\hat{R} = x\hat{x} + y\hat{y}$ spans this transverse plane; the position vector in three dimensions is $\boldsymbol{r} = x\hat{x} + y\hat{y} + z\hat{z} = \boldsymbol{R} + z\hat{z}$. A plane wave distribution is denoted by the Fourier spectral density $\boldsymbol{E}(\Omega, \boldsymbol{K})$. In an infinite medium with no sources, the field resulting from the superposition of such plane waves that together with the associated magnetic field, satisfies the Maxwell equations takes the form:

$$\boldsymbol{\mathcal{E}}(\boldsymbol{r}, t) = \int_0^\infty \frac{d\Omega}{2\pi} \int \frac{d\boldsymbol{K}}{(2\pi)^2} \boldsymbol{E}(\Omega, \boldsymbol{K}; z) e^{i\boldsymbol{K}\cdot\boldsymbol{R}} e^{-i\Omega t} + \text{c.c.} \tag{1}$$

where

$$\boldsymbol{E}(\Omega, \boldsymbol{K}; z) = \boldsymbol{E}_+(\Omega, \boldsymbol{K}; z) + \boldsymbol{E}_-(\Omega, \boldsymbol{K}; z), \tag{2}$$

$$\boldsymbol{E}_\pm(\Omega, \boldsymbol{K}; z) = \boldsymbol{E}_\pm(\Omega, \boldsymbol{K}) e^{\pm iwz}, \tag{3}$$

$$\boldsymbol{E}_\pm(\Omega, \boldsymbol{K}) = \hat{s} E_\pm^s(\Omega, \boldsymbol{K}) + \hat{p}_\pm E_\pm^{p\pm}(\Omega, \boldsymbol{K}), \tag{4}$$

where a subscript $\pm$ is now used to denote the $\pm\hat{z}$ direction in which the field is either propagating or suffering evanescent decay with wavenumber component $\pm w$ along the axial direction. We refer generally to the $+$ ($-$) component as the upward (downward) propagating wave. For example, the distribution representing an upward propagating plane wave of complex amplitude $\boldsymbol{E}_+^{\Omega_\circ, \boldsymbol{K}_\circ}$ at $z = z_\circ$ would be represented by

$$\boldsymbol{E}_+(\Omega, \boldsymbol{K}; z_\circ) = \boldsymbol{E}_+^{\Omega_\circ, \boldsymbol{K}_\circ} \delta(\Omega - \Omega_\circ) \delta(\boldsymbol{K} - \boldsymbol{K}_\circ), \tag{5}$$

where $\delta(x)$ denotes the Dirac delta distribution. The wave and polarization vectors are sketched on Fig. 1 for a situation in which they are real. More generally, in an isotropic

medium, they are given by:

$$\boldsymbol{\nu}_\pm \equiv \boldsymbol{K} \pm w\hat{z}, \tag{6}$$

$$w \equiv \left(\tilde{\Omega}^2 n^2 - K^2\right)^{1/2}, \tag{7}$$

$$\hat{s} \equiv \hat{K} \times \hat{z}, \tag{8}$$

$$\hat{p}_\pm \equiv \nu^{-1}\left(K\hat{z} \mp w\hat{K}\right), \tag{9}$$

where $\boldsymbol{\nu}_\pm = \nu\hat{\nu}_\pm$ is the wave vector with the wave number $\nu = \tilde{\Omega}n$, $\tilde{\Omega} \equiv \Omega/c$ with c the speed of light, n is the (in general complex) index of refraction, $\boldsymbol{K} = K\hat{K}$ is the transverse component of the wave vector, and square roots of complex numbers z are defined such that $\mathrm{Im}\sqrt{z} \geq 0$, and $\mathrm{Re}\sqrt{z} \geq 0$ if $\mathrm{Im}\sqrt{z} = 0$. Throughout we will use subscripts, such as in w_i and $\hat{p}_{i\pm}$, to denote the indicated parameters in a medium of refractive index n_i. It should be noted that, for an upward propagating plane wave, given Ω and $\boldsymbol{K}$, one knows the direction $\hat{\nu}_{i\pm}$ of the propagation vector through Eqs. (6) and (7), and that the direction depends on the index of refraction of the medium n_i.

3. Propagation and Transformations

In realistic experimental geometries, THz pulses propagate through air, dielectric media, and collimating optics. Since we are interested in the linear propagation of THz pulses, we can describe the transformation of a single plane wave through such media and optics, and reconstruct the transformation of a THz pulse from a superposition of plane waves. We now introduce the necessary transformations of plane waves through dielectric media and through lenses.

A. Free space and dielectrics

In vacuum, dielectric, or any layered media where the interfaces are parallel to the xy plane, a plane wave always remains a plane wave or a sum of plane waves with the same wave vector

component $\boldsymbol{K}$. The propagation of the fields is facilitated by the use of transfer matrices. A host of conventions are in common use[16]. For positive frequency Ω, we find it convenient to define the matrices with respect to formal vectors $e_i(z)$ of the form:

$$e_i(z) = \begin{bmatrix} E_+(\Omega, \boldsymbol{K}) e^{iw_i z} \\ E_-(\Omega, \boldsymbol{K}) e^{-iw_i z} \end{bmatrix}, \tag{10}$$

where we consider a medium with an index of refraction n_i. Here $E_\pm(\Omega, \boldsymbol{K})$ identifies either $E^s_\pm(\Omega, \boldsymbol{K})$ or $E^{p\pm}_\pm(\Omega, \boldsymbol{K})$. Separate formal vectors $e_i(z)$ are used for $\hat{s}$- and $\hat{p}$-polarized light, since the effect of interfaces on the propagation of those two polarizations can be treated independently. The transfer matrix $M_i(z)$ that transforms the formal vector of Eq. (10) upon propagation in a uniform isotropic medium is:

$$M_i(z) = \begin{bmatrix} e^{iw_i z} & 0 \\ 0 & e^{-iw_i z} \end{bmatrix}, \tag{11}$$

i.e., $e_i(z_1) = M_i(z_1 - z_2) e_i(z_2)$ if z_1 and z_2 are in the same medium. The matrix M_{ij} for the passage through an interface separating media i and j takes the same form for either $\hat{s}$- or $\hat{p}$-polarized radiation; it is:

$$M_{ij} = \frac{1}{t_{ij}} \begin{bmatrix} 1 & r_{ij} \\ r_{ij} & 1 \end{bmatrix}, \tag{12}$$

i.e., $e_i(z_\circ^+) = M_{ij} e_j(z_\circ^-)$ if medium i exists at $z > z_\circ$ and medium j at $z < z_\circ$, where the Fresnel coefficients for $\hat{s}$ and $\hat{p}$ polarizations are:

$$r^p_{ij} = \frac{w_i n_j^2 - w_j n_i^2}{w_i n_j^2 + w_j n_i^2}, \quad r^s_{ij} = \frac{w_i - w_j}{w_i + w_j}, \tag{13}$$

$$t^p_{ij} = \frac{2 n_i n_j w_i}{w_i n_j^2 + w_j n_i^2}, \quad t^s_{ij} = \frac{2 w_i}{w_i + w_j}. \tag{14}$$

Now that basic propagation in dielectric media has been described, we shall examine the case where a lens is in the path of the beam.

B. Thin Lens

If the refractive index of a lens is not too large and if the lens is not too small, a good approximation of the effect of the lens on a beam of light is achieved by modelling it as a phase mask locally affecting each ray that propagates through it[17]. Consider first a wave distribution incident from $z < d_o$ with Fourier spectrum $\boldsymbol{E}_+(\Omega, \boldsymbol{K}; d_o^-) = \boldsymbol{E}_+^{\Omega_\circ, \boldsymbol{K}_\circ} \delta(\Omega - \Omega_\circ)\delta(\boldsymbol{K} - \boldsymbol{K}_\circ)$ at $z = d_o^-$ on a parabolic lens of total thickness D_L, width $2L$, radius of curvature $\tilde{R} = R_\circ$ and index of refraction n, as shown on Fig. 2. Recall this represents a plane wave with transverse wave vector $\boldsymbol{K}_\circ$, frequency $\Omega_\circ$, and vector amplitude $\boldsymbol{E}_+^{\Omega_\circ, \boldsymbol{K}_\circ}$. The thickness of the lens as a function of radial distance is $d_{\text{lens}}(R) = D_L - R^2/2\tilde{R}$ if $R < L$ and 0 if $R > L$, with a corresponding distance in vacuum $d_{\text{vac}}(R) = R^2/2\tilde{R}$ if $R < L$ and D_L if $R > L$. Hence, within the usual approximations[17], at $z = d_o + D_L$, the input plane wave has acquired a phase as a function of radial distance R and is now described by:

$$\boldsymbol{\mathcal{E}}(\boldsymbol{R} + (d_o + D_L)\hat{z}, t) = \boldsymbol{E}_+^{\Omega_\circ, \boldsymbol{K}_\circ} e^{iw_{\text{vac}} d_{\text{vac}}(\boldsymbol{R}) + iw_{\text{lens}} d_{\text{lens}}(\boldsymbol{R}) + i\boldsymbol{K}_\circ \cdot \boldsymbol{R} - i\Omega_\circ t} + \text{c.c.} \tag{15}$$

with w_{lens} (w_{vac}) being the z-component of the wave vector inside (outside) the lens material. Reflections from any of the interfaces as well as polarization dependent refraction effects are neglected. The output wave is clearly no longer a plane wave because of the R-dependence imprinted on its phase. Thus, at $z = d_o + D_L$, an incident plane wave of transverse wave vector $\boldsymbol{K}_\circ$ has become a distribution of plane waves $\boldsymbol{E}_+(\Omega, \boldsymbol{K}'; d_o + D_L)$:

$$\boldsymbol{\mathcal{E}}(\boldsymbol{R} + (d_o + D_L)\hat{z}, t) = \int_o^\infty \frac{d\Omega}{2\pi} \int \frac{d\boldsymbol{K}'}{(2\pi)^2} \boldsymbol{E}_+(\Omega, \boldsymbol{K}'; d_o + D_L)\, e^{i\boldsymbol{K}' \cdot \boldsymbol{R} - i\Omega t} + \text{c.c.} \tag{16}$$

with

$$\boldsymbol{\mathcal{E}}(\boldsymbol{R} + (d_o + D_L)\hat{z}, t) = \begin{cases} \boldsymbol{E}_+^{\Omega_\circ, \boldsymbol{K}_\circ} e^{-i\Delta w R^2/2\tilde{R} + iw_{\text{lens}} D_L + i\boldsymbol{K}_\circ \cdot \boldsymbol{R} - i\Omega_\circ t} + \text{c.c.} & \text{for } R < L \\ \boldsymbol{E}_+^{\Omega_\circ, \boldsymbol{K}_\circ} e^{iw_{\text{vac}} D_L + i\boldsymbol{K}_\circ \cdot \boldsymbol{R} - i\Omega_\circ t} + \text{c.c.} & \text{for } R > L, \end{cases} \tag{17}$$

where $\Delta w = w_{\rm lens} - w_{\rm vac}$. One easily extracts the distribution $\boldsymbol{E}_+(\Omega, \boldsymbol{K}'; d_o + D_L)$ with an inverse Fourier transform of Eqs (15) and (16):

$$\begin{aligned}\boldsymbol{E}_+(\Omega, \boldsymbol{K}'; d_o + D_L) \;=\; & \boldsymbol{E}_+^{\Omega_\circ, \boldsymbol{K}_\circ}\delta(\Omega - \Omega_\circ)\;\left\{e^{iw_{\rm lens}D_L}\int_{R<L} d\boldsymbol{R}e^{i(\boldsymbol{K}_\circ - \boldsymbol{K}')\cdot\boldsymbol{R} - i\Delta w R^2/2\tilde{R}}\right. \\ & \left. + e^{iw_{\rm vac}D_L}\int_{R>L} d\boldsymbol{R}e^{i(\boldsymbol{K}_\circ - \boldsymbol{K}')\cdot\boldsymbol{R}}\right\}. \end{aligned} \tag{18}$$

As can be seen from Eq. (18), a single plane wave will exhibit diffraction rings after it has propagated through the lens due to the effect of the edge of the lens. Similarly, superpositions of plane waves that result in spatial profiles larger than the lens itself will not be properly focussed or collimated and will therefore be attenuated. We can simplify the mathematical expressions and keep essentially the same attenuation effect as Eq. (18) if, instead of a finite lens of half-width L, a Gaussian aperture (or soft aperture) of 1/e half width $\sqrt{2}L$ (in amplitude) is assumed. The width of the soft aperture is defined such that the energy of a plane wave after the lens is the same as what it would be were it a hard aperture. One can easily show that Eq. (15) with a complex radius of curvature

$$\frac{1}{\tilde{R}} = \frac{1}{R_\circ} - \frac{i}{\Delta w L^2}, \tag{19}$$

represents a Gaussian aperture of half width $\sqrt{2}L$, with $R_\circ$ the real radius of curvature of the lens. Using the shorthand notation

$$K_L^2 = \frac{2\Delta w}{R_\circ} - \frac{2i}{L^2}, \tag{20}$$

equation (18) can then be approximated by:

$$\boldsymbol{E}_+(\Omega, \boldsymbol{K}'; d_o + D_L) \;\approx\; \boldsymbol{E}_+^{\Omega_\circ, \boldsymbol{K}_\circ}\delta(\Omega - \Omega_\circ)e^{i\Delta w D_L}\int d\boldsymbol{R}e^{i(\boldsymbol{K}_\circ - \boldsymbol{K}')\cdot\boldsymbol{R}}e^{-i\frac{R^2K_L^2}{4}}, \tag{21}$$

$$= \frac{4\pi i}{K_L^2}\boldsymbol{E}_+^{\Omega_\circ, \boldsymbol{K}_\circ}\delta(\Omega - \Omega_\circ)e^{i\frac{|\boldsymbol{K}_\circ - \boldsymbol{K}'|^2}{K_L^2} + i\Delta w D_L}, \tag{22}$$

where the integral has been performed using the identity[18]:

$$\int_0^{2\pi} d\phi e^{im\phi} e^{ix\cos\phi} = 2\pi i^m J_m(x), \tag{23}$$

with $J_m(x)$ the Bessel function of order m, as well as

$$\int_0^{\infty} R\, dR\, e^{iaR^2} J_0(bR) = \frac{i}{2a} e^{\frac{-ib^2}{4a}}. \tag{24}$$

If a distribution of waves $\boldsymbol{E}_+(\Omega, \boldsymbol{K}; d_o^-)$ is incident on the lens, the resulting distribution behind the lens is obtained by superposition:

$$\boldsymbol{E}_+\left(\Omega, \boldsymbol{K}'; d_o^+\right) = \frac{4\pi i}{K_L^2} \int \frac{d\boldsymbol{K}}{(2\pi)^2} \boldsymbol{E}_+\left(\Omega, \boldsymbol{K}; d_o^-\right) e^{i\frac{|\boldsymbol{K}-\boldsymbol{K}'|^2}{K_L^2}}, \tag{25}$$

where we have taken the thin lens limit where $D_L \to 0^+$. Equations (20) and (25) can be used to implement the lens transformation numerically. However, it will be shown in section 5 that the transformation corresponding to a common experimental geometry, where a Gaussian beam is collimated and refocused, can be treated analytically.

4. Sources, Green Function and Geometry

Although we have described the propagation of THz radiation in dielectric media and lenses, we have not discussed the generation of the radiation itself. From standard electromagnetism theory, it is known that electromagnetic fields are radiated from oscillating currents. With any current density $\boldsymbol{\mathcal{J}}(\boldsymbol{r}, t)$, we can associate a polarization potential (or density) according to $\boldsymbol{\mathcal{J}}(\boldsymbol{r}, t) = \dfrac{\partial \boldsymbol{\mathcal{P}}(\boldsymbol{r}, t)}{\partial t}$. Obtaining the radiated electric field for a given polarization density $\boldsymbol{\mathcal{P}}(\boldsymbol{r}, t)$ is a boundary condition problem and depends on the geometry of the system under study. For instance, if the source $\boldsymbol{\mathcal{P}}(\boldsymbol{r}, t)$ is embedded in a dielectric medium with interfaces to other media, there will be multiple Fresnel reflections of the generated waves that will interfere inside and outside the dielectric material and affect the resulting radiation spectrum

and profile. If the polarization source is described in terms of $\boldsymbol{P}(\Omega, \boldsymbol{K}; z)$ such that:

$$\boldsymbol{\mathcal{P}}(\boldsymbol{r}, t) = \int_0^\infty \frac{d\Omega}{2\pi} \int \frac{d\boldsymbol{K}}{(2\pi)^2} \boldsymbol{P}(\Omega, \boldsymbol{K}; z) e^{i\boldsymbol{K}\cdot\boldsymbol{R}} e^{-i\Omega t} + \text{c.c.}, \tag{26}$$

the radiated field is obtained in general from the following Green function integral:

$$\boldsymbol{E}(\Omega, \boldsymbol{K}; z) = \int dz' \overleftrightarrow{G}(\Omega, \boldsymbol{K}; z - z') \cdot \boldsymbol{P}(\Omega, \boldsymbol{K}; z'). \tag{27}$$

In an infinite medium of index n_1, the Green function, in "MKS units", is[15]:

$$\begin{aligned} \overleftrightarrow{G}(\Omega, \boldsymbol{K}; z) \;=\; & \frac{i\tilde{\Omega}^2}{2\epsilon_\circ w_1} (\hat{s}\hat{s} + \hat{p}_{1+}\hat{p}_{1+}) \theta(z) e^{iw_1 z} \\ & + \frac{i\tilde{\Omega}^2}{2\epsilon_\circ w_1} (\hat{s}\hat{s} + \hat{p}_{1-}\hat{p}_{1-}) \theta(-z) e^{-iw_1 z} \\ & - \frac{1}{n_1^2 \epsilon_\circ} \hat{z}\hat{z}\delta(z), \end{aligned} \tag{28}$$

with the Heaviside function $\theta(z) = 1, 0$ for $z > 0, < 0$ and $\epsilon_\circ$ the permittivity of free space. The right hand side of Eq. (28) has terms representing the upward ($e^{iw_1 z}$) and downward ($e^{-iw_1 z}$) propagating (or evanescent) waves originating from a polarization density $\boldsymbol{P}(\Omega, \boldsymbol{K}; z')$ at z' for both $\hat{s}$ and $\hat{p}_{1\pm}$ polarizations, as well as a local term that will not be relevant for this work and that has been discussed earlier[15]. For an arbitrary geometry with a source embedded in a dielectric, the results from section 3 are used to obtain the Green function for any polarization source embedded in any layered dielectric structure. A common geometry is shown in Fig. 3, where two semi-infinite dielectric materials with indices of refraction n_1 and n_2 (which can be frequency-dependent) are on either side of a third material with index of refraction n_3 and thickness D. When the polarization source is contained in medium 3, the expression for the upward propagating radiation in medium 1 for $z > 0$ is given by[15]:

$$\begin{aligned} \boldsymbol{E}_+(\Omega, \boldsymbol{K}; z) \;=\; & \frac{i\tilde{\Omega}^2}{2\epsilon_\circ w_3} \sum_{\hat{q}} \mathcal{C}^q e^{iw_1 z} \left[\hat{q}_{1+}\hat{q}_{3+} \cdot \int_{-D}^0 dz' e^{-iw_3 z'} \boldsymbol{P}(\Omega, \boldsymbol{K}; z') \right. \\ & \left. + r_{32}^q e^{2iw_3 D} \hat{q}_{1+}\hat{q}_{3-} \cdot \int_{-D}^0 dz' e^{iw_3 z'} \boldsymbol{P}(\Omega, \boldsymbol{K}; z') \right] \end{aligned} \tag{29}$$

which is expressed as a sum over polarization states $\hat{q} = \{\hat{s}, \hat{p}\}$ in medium i, where $\hat{s}_+ = \hat{s}_- \equiv \hat{s}$. The Fabry-Perot term for $\hat{s}$ and $\hat{p}$ polarizations is:

$$\mathcal{C}^q = \frac{t^q_{31}}{1 - r^q_{32} r^q_{31} e^{i2w_3 D}}, \tag{30}$$

where t^q_{ij} and r^q_{ij} are the Fresnel coefficients for that polarization. At any point, the full electric field in space and time is obtained by applying a Fourier transform back into real time t and real space $\boldsymbol{r}$. The full broadband field can be written explicitly from Eq. (1) and its explicit calculation for different geometries and sources is the object of the next section.

Expressions for the calculation of the radiation profile, using Eq. (1) together with (27) and the appropriate Green function, can be simplified when what is wanted is the temporal profile far from the polarization source $\boldsymbol{P}(\Omega, \boldsymbol{K}; z)$. To that end, it is useful to rewrite expansions of the form (1) involving $\boldsymbol{E}_+(\Omega, \boldsymbol{K}; z)$ as:

$$\boldsymbol{\mathcal{E}}(\boldsymbol{r}, t) = \int_0^\infty \frac{d\Omega}{2\pi} \int \frac{i d\boldsymbol{K}}{2\pi w} \boldsymbol{e}_+(\Omega, \boldsymbol{K}) e^{iwz} e^{i\boldsymbol{K}\cdot\boldsymbol{R} - i\Omega t} + \text{c.c.}, \tag{31}$$

where

$$\boldsymbol{e}_+(\Omega, \boldsymbol{K})\, e^{iwz} = -\frac{iw}{2\pi} \boldsymbol{E}_+(\Omega, \boldsymbol{K}; z)\,. \tag{32}$$

The far field limit, as $r \to \infty$ with $z > 0$ and $\hat{r} = \boldsymbol{r}/r$ fixed, is[19]:

$$\boldsymbol{\mathcal{E}}(\boldsymbol{r}, t) \sim \int_0^\infty \frac{d\Omega}{2\pi} \boldsymbol{e}_+(\Omega, \bar{\boldsymbol{K}}) \frac{e^{i\tilde{\Omega} n r - i\Omega t}}{r} + \text{c.c.}, \tag{33}$$

where the value of w and n are calculated in the medium where the wave is propagating in the far field, and $\bar{\boldsymbol{K}} = \nu \hat{r} \cdot (\overleftrightarrow{U} - \hat{z}\hat{z})$ with $\overleftrightarrow{U}$ the unit tensor . Clearly, the Fourier component with wave vector $\bar{\boldsymbol{K}}$ dominates for a given $\hat{r}$ and frequency Ω. For instance, if one looks at the beam at a far distance z in the direction of the $\hat{z}$ axis, then $\hat{r} = \hat{z}$, and $\bar{\boldsymbol{K}} = \nu \hat{z} \cdot (\overleftrightarrow{U} - \hat{z}\hat{z}) = \boldsymbol{0}$.

5. Examples

We first discuss how to calculate the temporal profile for an infinite medium with Eq. (1). The integral over Ω is a simple Fourier transform, but the integral over $\boldsymbol{K}$ in Eq. (1) is complicated because of the vector nature of $\boldsymbol{K}$. The product $\boldsymbol{K}\cdot\boldsymbol{R}$, the arbitrary distribution $\boldsymbol{P}(\Omega,\boldsymbol{K};z)$, and the implicit dependence of $\hat{s}$ and $\hat{p}_{\pm}$ on $\boldsymbol{K}$ (see Eqs 8 and 9) make the integral over the orientation of $\boldsymbol{K}$ non-trivial, except for the the far field case where Eq. (33) can be used. Moreover, in general, the radiated field $\boldsymbol{\mathcal{E}}(\boldsymbol{r},t)$ has components along all three Cartesian coordinates even if $\boldsymbol{P}(\Omega,\boldsymbol{K};z)$ is linearly polarized. Therefore, before explicitly integrating Eq. (1), it is useful to make appropriate assumptions on the polarization source $\boldsymbol{P}(\Omega,\boldsymbol{K};z)$, as well as to restrict ourselves to the component of interest of the radiated field.

As our examples, we calculate the temporal profile of the electric field component polarized along $\hat{x}$, at $R=0$ (*i.e.*, on the $\hat{z}$ axis) for the upward propagating wave originating from a polarization source $\boldsymbol{\mathcal{P}}(\boldsymbol{r},t)$. Also, we take the polarization source $\boldsymbol{\mathcal{P}}(\boldsymbol{r},t)$ to be cylindrically symmetric and linearly polarized along $\hat{x}$ thereby making the polarization density simple to describe and the integrals easy to evaluate. These approximations correspond to most experimental situations in the literature today, and illustrate all features of the formalism.

To illustrate the results with an analytically simple case, we first consider a cylindrically symmetric sheet of polarization

$$\boldsymbol{P}(\Omega,\boldsymbol{K};z)=\hat{x}P(\Omega,K)\delta(z) \tag{34}$$

embedded in a uniform medium of index of refraction n_1.

A. *Asymptotic expression for far field*

A simple expression for the far field temporal profile from the polarization sheet (34) can be obtained using the Green function (28) for an infinite medium in the general expression for the field (27), and substituting the field in the far field limit (33). For an observation point on the $\hat{z}$ axis (*i.e.*, $\boldsymbol{r} = z\hat{z}$ and therefore $\bar{\boldsymbol{K}} = \boldsymbol{0}$), the $\hat{x}$ component of the field is given by:

$$\hat{x} \cdot \boldsymbol{\mathcal{E}}(z\hat{z}, t) \sim \frac{1}{4\pi\epsilon_\circ z} \int_0^\infty \frac{d\Omega}{2\pi} \tilde{\Omega}^2 P(\Omega, 0) e^{i\tilde{\Omega} n_1 z - i\Omega t} + \text{c.c.} \tag{35}$$

The results for a polarization with a Gaussian spectrum and a Gaussian spatial profile

$$P(\Omega, K) = \frac{4\pi^{3/2}}{\sigma_\Omega \sigma_K^2} P_\circ e^{-\Omega^2/\sigma_\Omega^2} e^{-K^2/\sigma_K^2} \tag{36}$$

are shown on Fig. 4 for z = 50 mm in local time $t' = t - z\mathrm{Re}(n_1)/c$, where $\mathrm{Re}(n_1)$ is the real part of the index of refraction and $P_\circ$ the peak polarization density. The far field profile follows the time derivative of the current $\dfrac{\partial \boldsymbol{\mathcal{J}}}{\partial t} = \dfrac{\partial^2 \boldsymbol{\mathcal{P}}}{\partial t^2}$, as can be seen from the figure. Alternatively, this can be seen directly from Eq. (35), since the temporal Fourier transform of the time derivative of the current is proportional to $\Omega^2 P(\Omega, K)$.

B. *Near and far fields*

In general, the detector must be sufficiently far from the source for the asymptotic limit (35) to be adequate. If this is not the case, then one must integrate Eq. (1). The integral over $\boldsymbol{K}$ is written out as a 2D integral in cylindrical coordinates with $K = |\boldsymbol{K}|$ and ϕ the angle between the $\hat{x}$ axis and the vector $\boldsymbol{K}$. All dyadics of the form $\hat{a}\hat{b}$, where $\hat{a}$ and $\hat{b}$ are $\hat{s}$ or one of the $\hat{p}$'s, are expanded in the form:

$$\hat{a}\hat{b} = \sum_m \overleftrightarrow{f}_m \left(\hat{a}\hat{b}\right) e^{-im\phi} \tag{37}$$

where only a finite number of coefficients $\overleftrightarrow{f}_m \left(\hat{a}\hat{b}\right)$ survive ($m = \pm 2, \pm 1, 0$). These are easily determined and are given in Appendix A. The integral over ϕ can then be performed analytically, whereas the remaining integrals over Ω and K are performed numerically. This reduces

considerably both the computing time and the memory requirements for the computation, making the results developed here very easily handled by a modest personal computer.

To obtain the x component of the upward propagating field in the case of a polarization sheet (34) in an infinite medium, Eqs (27) and (28) are used:

$$\hat{x}\cdot\boldsymbol{E}_{+}(\Omega,\boldsymbol{K};z)=\frac{i\tilde{\Omega}^{2}}{2\epsilon_{\circ}w_{1}}\left(\sum_{m}\left[\overleftrightarrow{f}_{m}\left(\hat{s}\hat{s}\right)+\overleftrightarrow{f}_{m}\left(\hat{p}_{1+}\hat{p}_{1+}\right)\right]e^{-im\phi}\right)\cdot\hat{x}e^{iw_{1}z}P(\Omega,K). \tag{38}$$

The $\hat{x}$ component of $\boldsymbol{E}_{+}(\Omega,\boldsymbol{K};z)$ follows from the use of the $\overleftrightarrow{f}_{m}$ given in Appendix A:

$$\hat{x}\cdot\boldsymbol{E}_{+}(\Omega,\boldsymbol{K};z)=\frac{i\tilde{\Omega}^{2}}{2\epsilon_{\circ}w_{1}}\left(\frac{1}{2}-\frac{1}{2}\cos 2\phi+\frac{w_{1}^{2}}{2\nu_{1}^{2}}+\frac{w_{1}^{2}}{2\nu_{1}^{2}}\cos 2\phi\right)e^{iw_{1}z}P(\Omega,K). \tag{39}$$

To obtain the temporal profile of the THz field, we substitute Eq (39) in Eq. (1) and integrate over ϕ, Ω, and K; the first integral is done analytically. For an observation point at $\boldsymbol{r}=z\hat{z}$ (*i.e.*, on axis), we obtain:

$$\hat{x}\cdot\boldsymbol{\mathcal{E}}(z\hat{z},t)\;=\;\frac{i}{2\epsilon_{\circ}}\int_{0}^{\infty}\frac{d\Omega}{2\pi}\tilde{\Omega}^{2}e^{-i\Omega t}\int_{0}^{\infty}\frac{KdK}{2\pi}\left(\frac{1}{2}+\frac{w_{1}^{2}}{2\nu_{1}^{2}}\right)w_{1}^{-1}e^{iw_{1}z}P(\Omega,K). \tag{40}$$

When a broad range of wave vectors $\boldsymbol{K}$ is present, w_1 can decrease to a very small value or even become imaginary. If n_1 is real, the divergence w_1^{-1} is purely formal since it can be integrated over and can easily be handled analytically. In practice, however, any residual absorption in medium 1 will ensure that w_1 never vanishes (see Eq. 7). The integrand is then strongly peaked but can be integrated numerically with appropriate sampling. The integrand is sampled at different values of $K\left[i\right]$ where $w_1(\Omega,K\left[i+1\right])-w_1(\Omega,K\left[i\right])$ is constant and equal to Δ, as long as the corresponding change in $K\left[i+1\right]-K\left[i\right]$ is smaller than Δ. The sampling parameter Δ is decreased appropriately until the calculated results do not change. Results for a polarization of the type of Eq. (36) are shown on Fig. 5 in local time $t'=t-z\mathrm{Re}(n_1)/c$ and at different z values. We see the onset of the asymptotic solution Eq. (35) as the distance from the source is increased. The radiated field follows

the current or the time derivative of the polarization $\boldsymbol{\mathcal{J}} = \dfrac{\partial \boldsymbol{\mathcal{P}}}{\partial t}$ close to the source but is reshaped into the time derivative of the current density $\dfrac{\partial \boldsymbol{\mathcal{J}}}{\partial t} = \dfrac{\partial^2 \boldsymbol{\mathcal{P}}}{\partial t^2}$ in the far field, as was obtained in Fig. 4.

6. Experimental geometries and sources

To extend the previous results to experimentally interesting geometries and polarization sources is straightforward. The geometry of Fig. 3, often encountered in experiments, is considered. For the purpose of example, we consider a linearly-polarized, cylindrically-symmetric, optically-generated polarization source, as obtained from below band gap second-order rectification[6,14,20]. The source substrate of thickness $D = 100$ μm is (110)-oriented GaAs and is surrounded by air (*i.e.*, $n_1 = n_2 = 1$), as shown on Fig. 3. The only non-zero second-order susceptibility coefficients of GaAs are $\chi_2^{(xyz)} = 100$ pmV^{-1}, where (xyz) is any permutation of xyz. The frequency-dependent index of refraction $n_3(\Omega)$ of GaAs is obtained from experimental data[21]. The optical pump beam is assumed normally incident from $z < -D$ on the GaAs (medium 3). The spectrum of an optical pump beam centered at $\omega_\circ$ with a Gaussian spatial profile is described (see Eq. 3) by:

$$E_+(\omega, \boldsymbol{K}) e^{-i\omega_\circ D/c} = \frac{4\pi^{3/2}}{\sigma_{\omega_\circ} \sigma_{\kappa_\circ}^2} E_{\omega_\circ} e^{-(\omega-\omega_\circ)^2/\sigma_{\omega_\circ}^2} e^{-|\boldsymbol{K}|^2/\sigma_{\kappa_\circ}^2}, \tag{41}$$

with a positive center frequency of $2\pi c \omega_\circ^{-1} = 1.55$ μm, a spectral width of $2\sigma_{\omega_\circ}^{-1} = 125$ fs, and a spot $1/e$-width of 100 μm, giving $2\sigma_{\kappa_\circ}^{-1} = 100$ μm with a peak intensity inside the crystal of $2\left|E_{\omega_\circ}\right|^2 n_3/Z_\circ = 5$ GWcm^{-2} with $Z_\circ = 377$ Ohms the vacuum impedance. Neglecting diffraction of the optical pump beam, the following polarization density $\boldsymbol{P}(\Omega, \boldsymbol{K}; z)$ results:

$$\boldsymbol{P}(\Omega, \boldsymbol{K}; z) \;=\; \hat{x} P(\Omega, K)\, e^{(i n_{\omega_\circ}^g \tilde{\Omega} - 2\alpha_{\omega_\circ})(z+D)}, \tag{42}$$

with

$$P(\Omega, K) = 2\epsilon_\circ \chi_2^{\text{eff}} \left|E_{\omega_\circ}\right|^2 \frac{4\pi^{3/2}}{\sigma_{\omega_\circ}\sigma_{\kappa_\circ}^2} e^{-\Omega^2/\sigma_\Omega^2} e^{-K^2/\sigma_K^2}. \tag{43}$$

Here, $\chi_2^{\text{eff}} = \chi_2^{(xyz)}/2$ is the effective nonlinear susceptibility with the optical pump fields polarized along $\hat{y}$ ($\bar{1}10$), $\sigma_\Omega = \sqrt{2}\sigma_{\omega_\circ}$ and $\sigma_K = \sqrt{2}\sigma_{k_\circ}$ are the spectral widths in frequency space Ω and transverse wave vector space $\boldsymbol{K}$ respectively, $n_{\omega_\circ}^g = 3.1$ is the pump group index and $\alpha_{\omega_\circ}$ is the field absorption coefficient at the pump frequency $\omega_\circ$.

A. Asymptotic expression for far field

To obtain the far field radiation propagating in the positive $\hat{z}$ direction in the medium 1, we substitute the polarization (42) into the expression for the field (29) and use the result in Eq. (32) to obtain:

$$\begin{aligned} \boldsymbol{e}_+(\Omega, \boldsymbol{K}) \;=\; & \frac{\tilde{\Omega}^2}{4\pi\epsilon_\circ} \sum_{\hat{q}} \mathcal{C}^q \left[\hat{q}_{3+} \cdot \int_{-D}^{0} dz' e^{-iw_3 z'} \boldsymbol{P}(\Omega, \boldsymbol{K}; z') \right. \\ & \left. + r_{32}^q e^{2iw_3 D} \hat{q}_{3-} \cdot \int_{-D}^{0} dz' e^{iw_3 z'} \boldsymbol{P}(\Omega, \boldsymbol{K}; z') \right], \end{aligned} \tag{44}$$

which we substitute into the general expression for the far field (33). The integral over z' can be performed analytically and written as:

$$\begin{aligned} \int dz' e^{\mp iw_3 z'} \boldsymbol{P}(\Omega, \boldsymbol{K}; z') \;&=\; \hat{x} P(\Omega, K) \int_{-D}^{0} dz' e^{(in_{\omega_\circ}^g \tilde{\Omega} - 2\alpha_{\omega_\circ})(z+D)} e^{\mp iw_3 z'} && (45) \\ &\equiv\; \hat{x} P(\Omega, K)\, L_\pm(\Omega, K), && (46) \end{aligned}$$

where $L_\pm(\Omega, K)$ is the effective interaction length for the upward- and downward-propagating waves:

$$L_\pm(\Omega, K) = \left[\frac{e^{in_{\omega_\circ}^g \tilde{\Omega} D - 2\alpha_{\omega_\circ} D} - e^{\pm iw_3 D}}{\mp iw_3 + in_{\omega_\circ}^g \tilde{\Omega} - 2\alpha_{\omega_\circ}} \right] \tag{47}$$

and grows in magnitude as the fields approach the usual phase-matching condition. For an observation point on the $\hat{z}$ axis (*i.e.*, $\boldsymbol{r} = z\hat{z}$ and therefore $\bar{\boldsymbol{K}} = \boldsymbol{0}$), the $\hat{x}$ component of the

temporal profile of the beam is:

$$\hat{x}\cdot\boldsymbol{\mathcal{E}}(z\hat{z},t)\ \sim\ \int\frac{d\Omega}{2\pi}\frac{\tilde{\Omega}^2}{4\pi\epsilon_\circ}\mathcal{C}^sP\left(\Omega,0\right)\left[L_+(\Omega,0)+r_{32}^se^{2iw_3D}L_-(\Omega,0)\right]\frac{e^{i\tilde{\Omega}nz-i\Omega t}}{z}+\text{c.c.},\quad(48)$$

where we took $\hat{x}\cdot\hat{s}=1$ and $\hat{x}\cdot\hat{p}=0$ to lift the ambiguity of Eqs (8) and (9) at $\bar{\boldsymbol{K}}=\mathbf{0}$. The results are shown on Fig. 6 at $z=5$ cm for the polarization source described by Eq. (42), with the same parameters as before except for a larger bandwidth $\sigma_\Omega/2\pi=3.8$ THz. This slightly overlaps the first phonon resonance at 8.5 THz in GaAs, which is implicitly included *via* $n_3(\Omega)$. Our results demonstrate how all the dispersive features of the source material are included in the calculation. The inset shows the corresponding spectrum amplitude where one can clearly see Fabry-Perot and phonon resonances, as well as the effects of the frequency-dependent interaction length (which is zero at 6.1 THz).

B. Near and far fields

An approach similar to that used to calculate the near field for the polarization sheet in the previous section is used here to calculate the near field temporal profile. Starting from Eq. (29), the $\hat{x}$ component of the field from both polarizations is:

$$\begin{aligned}\hat{x}\cdot\boldsymbol{E}_+\left(\Omega,\boldsymbol{K};z\right)\ =\ &\frac{i\tilde{\Omega}^2}{2\epsilon_\circ w_3}e^{iw_1z}\sum_{\hat{q}}\mathcal{C}^q\left[\int_{-D}^{0}dz'e^{-iw_3z'}\hat{x}\cdot\hat{q}_{1+}\hat{q}_{3+}\cdot\hat{x}P(\Omega,\boldsymbol{K};z')\right.\\&\left.+\,r_{32}^qe^{2iw_3D}\int_{-D}^{0}dz'e^{iw_3z'}\hat{x}\cdot\hat{q}_{1+}\hat{q}_{3-}\cdot\hat{x}P(\Omega,\boldsymbol{K};z')\right].\end{aligned}\quad(49)$$

Using the results of Appendix A, $\hat{x}\cdot\hat{q}_{1+}\hat{q}_{3+}\cdot\hat{x}$ and $\hat{x}\cdot\hat{q}_{1+}\hat{q}_{3-}\cdot\hat{x}$ are rewritten and we obtain the equation for the field:

$$\begin{aligned}\hat{x}\cdot\boldsymbol{E}_+\left(\Omega,\boldsymbol{K};z\right)\ =\ &\frac{i\tilde{\Omega}^2}{2\epsilon_\circ w_3}e^{iw_1z}P\left(\Omega,K\right)\\&\times\left[L_+(\Omega,K)\left(\frac{1}{2}\mathcal{C}^s-\frac{1}{2}\mathcal{C}^s\cos2\phi+\frac{w_1w_3}{2\nu_1\nu_3}\mathcal{C}^p+\frac{w_1w_3}{2\nu_1\nu_3}\mathcal{C}^p\cos2\phi\right)\right.\\&+e^{2iw_3D}L_-(\Omega,K)\left(\frac{1}{2}r_{32}^s\mathcal{C}^s-\frac{1}{2}r_{32}^s\mathcal{C}^s\cos2\phi\right.\\&\left.\left.-\frac{w_1w_3}{2\nu_1\nu_3}r_{32}^p\mathcal{C}^p-\frac{w_1w_3}{2\nu_1\nu_3}r_{32}^p\mathcal{C}^p\cos2\phi\right)\right].\end{aligned}\quad(50)$$

Finally, to obtain the total field, Eq. (1) is integrated over Ω and $\boldsymbol{K}$ with Eq. (50). The integral over ϕ, the orientation of $\boldsymbol{K}$, is performed analytically, leaving us with :

$$\hat{x}\cdot\boldsymbol{\mathcal{E}}(z\hat{z},t) = \int_0^\infty \frac{d\Omega}{2\pi}e^{-i\Omega t}\frac{i\tilde{\Omega}^2}{2\epsilon_\circ}\int_0^\infty \frac{KdK}{2\pi}w_3^{-1}e^{iw_1 z}P(\Omega,K)\left[\left(\frac{1}{2}\mathcal{C}^s+\frac{w_1w_3}{2\nu_1\nu_3}\mathcal{C}^p\right)L_+(\Omega,K)\right.$$
$$\left.+\,e^{2iw_3D}\left(\frac{1}{2}\mathcal{C}^s r_{32}^s-\frac{w_1w_3}{2\nu_1\nu_3}\mathcal{C}^p r_{32}^p\right)L_-(\Omega,K)\right]+\text{c.c.} \quad (51)$$

to integrate numerically. The integrand is strongly peaked as w_3 approaches zero and sampling of the function is done at different points $K[i]$ corresponding to a constant separation in w_3, as explained previously. The on-axis temporal profile of the THz radiation from below-band-gap optical rectification from a 100 μm substrate of GaAs is shown on Fig. 7. Multiple pulse reflections separated by 2.3 ps (as expected from the thickness of the substrate and its group index at THz frequencies) are observed. The pulses arising from the multiple reflections are increasingly chirped because of the dispersion of GaAs and the fact that the reflected pulses have travelled repeatedly through the sample.

C. Gaussian beam through finite size lens

We have shown in the previous sections how to calculate the near and far field temporal profiles of a THz beam as it propagates exclusively through layered media. However, because experimental THz radiation sources are often essentially point sources, diffraction is very important and the THz radiation must be collimated with optics for experiments. The dimensions of the optics are such that their finite clear aperture cannot collect all the energy of low frequencies of the THz spectrum that have diffracted to a size larger than the diameter of the collimating optics. Various experimental designs make use of off-axis parabolic mirrors (with a typical diameter of 2.5 cm) to collimate and focus THz beams. Their finite size has the effect of filtering out low frequencies while letting through the higher frequencies. Also, most THz detection systems make use of a *pair* of matched mirrors with

focal length f', set up far from the source and in such a way that the first one collimates a THz point source and the second one focuses it. Within the usual approximations[17], this particular arrangement can be treated as a single optical element of focal length $f = f'/2$, with $d_o = d_i = f'$ (see Fig. 8). We assume that these mirrors are adequately modelled by finite-size thin lenses as is usually assumed in optics[17] and it is therefore sufficient to study the case of a beam going through a single lens replacing the mirrors. The transformation of an arbitrary beam by the mirrors is then given by that of the lens in Eq. (25). This section is an example calculation using the results of section 3 B for the effect of finite-size mirrors on the spectrum and temporal profile of THz beams. In general, the results of the transformation depend on the spatial profile and radius of curvature of the beam at the entrance of the lens and is an imaging problem beyond the scope of this work. Therefore, we make the simplifying assumption that the input spatial profile is Gaussian, as is often the case experimentally.

We start with a linearly polarized Gaussian beam $\boldsymbol{E}_+(\Omega, \boldsymbol{K}) = 4\pi\sigma_K^{-2}\boldsymbol{E}_+(\Omega)\exp[-K^2/\sigma_K^2]$ at $z = 0$ with σ_K the (real) Gaussian width of the transverse wave vector distribution and $\boldsymbol{E}_+(\Omega) = \hat{x}E_+(\Omega)$ an arbitrary spectral density. At a distance d_o from its waist is a lens of focal length $f = R_\circ/(n-1)$, and we are interested in calculating the field at a distance d_i behind the lens (see Fig. 9). Using the paraxial wave approximation[22], the field immediately in front of the lens can be written as:

$$\boldsymbol{E}_+\left(\Omega, \boldsymbol{K}; d_o^-\right) = \boldsymbol{E}_+(\Omega, \boldsymbol{K})\, e^{i\tilde{\Omega}d_o - i\frac{K^2 d_o}{2\tilde{\Omega}}}. \tag{52}$$

A Gaussian spatial profile can therefore be written as:

$$\boldsymbol{E}_+\left(\Omega, \boldsymbol{K}; d_o^-\right) = \frac{4\pi}{\sigma_K^2}\boldsymbol{E}_+(\Omega)\, e^{i\tilde{\Omega}d_o} e^{-\frac{K^2}{\sigma_o^2(d_o)}} \tag{53}$$

with

$$\frac{1}{\sigma_o^2(d_o)} = \frac{1}{\sigma_K^2} + i\frac{d_o}{2\tilde{\Omega}}. \tag{54}$$

The lens transformation of Eq. (25) is performed with an input wave distribution of the form of Eq. (53) with the help of identities (23) and (24). We obtain the field immediately behind the lens with:

$$\boldsymbol{E}_+\left(\Omega, \boldsymbol{K}; d_o^+\right) = \frac{4\pi}{\sigma_K^2}\frac{\sigma_o^2(d_o)}{\sigma_o^2(d_o) + iK_L^2}\boldsymbol{E}_+(\Omega)e^{i\tilde{\Omega}d_o}e^{-\frac{K^2}{\sigma_o^2(d_o)+iK_L^2}}. \tag{55}$$

The propagation of the field by a distance d_i is then obtained simply by multiplying by e^{iwd_i} (see Eq. (11)):

$$\boldsymbol{E}_+\left(\Omega, \boldsymbol{K}; d_o + d_i\right) = \frac{4\pi}{\sigma_K^2}\frac{\sigma_o^2(d_o)}{\sigma_i^2(d_o, 0)}\boldsymbol{E}_+(\Omega)e^{i\tilde{\Omega}(d_o+d_i)}e^{-\frac{K^2}{\sigma_i^2(d_o,d_i)}}, \tag{56}$$

where we defined for simplicity:

$$\frac{1}{\sigma_i^2(d_o, d_i)} = \frac{1}{\sigma_o^2(d_o) + iK_L^2} + \frac{id_i}{2\tilde{\Omega}}. \tag{57}$$

When calculating the total field, for instance with Eq. (1), on the z axis (*i.e.*, $\boldsymbol{R} = \boldsymbol{0}$), and with polarization $\hat{x}$, the relative attenuation of frequency component Ω of the field at $z = d_o + d_i$ compared to the field at $z = 0$ is given by:

$$\mathcal{F}^{\text{full}}(\Omega, d_o, d_i) = \frac{\hat{x}\cdot\int\frac{d\boldsymbol{K}}{(2\pi)^2}\boldsymbol{E}_+\left(\Omega, \boldsymbol{K}; d_o + d_i\right)}{\hat{x}\cdot\int\frac{d\boldsymbol{K}}{(2\pi)^2}\boldsymbol{E}_+\left(\Omega, \boldsymbol{K}; 0\right)} = \frac{\sigma_o^2(d_o)}{\sigma_o^2(0)}\frac{\sigma_i^2(d_o, d_i)}{\sigma_i^2(d_o, 0)} \tag{58}$$

and its magnitude is shown on Fig. 10 for $\sigma_K^{-1} = 100$ μm, $L = 2.5$ cm, $f = 2.5$ cm, and $d_o = d_i = 5$ cm, corresponding to typical THz parameters. The lens acts as a low frequency filter. Low frequencies diffract more than do high frequencies and, therefore, their Gaussian spatial profile at the lens is wider than the lens itself and does not get fully collimated. Higher frequencies, on the other hand, do not diffract as much and are almost entirely collimated. This is entirely expected and can be understood intuitively with the following

physical argument. From previous results, we know that the far field in a given direction is related to a single transverse wave vector $\boldsymbol{K}$. Therefore, the finite clear aperture of the lens can be seen as collimating all waves that make an angle with the $\hat{z}$ axis smaller than θ_{co}, with $\tan\theta_{\mathrm{co}} = L/d_o \approx |\boldsymbol{K}_{\mathrm{co}}|/\tilde{\Omega}$ (see Fig. 9). Therefore, any plane wave component $\boldsymbol{E}_+(\Omega, \boldsymbol{K})$ with $|\boldsymbol{K}| < |\boldsymbol{K}_{\mathrm{co}}|$ goes through the collimating lens, whereas a component with $|\boldsymbol{K}| > |\boldsymbol{K}_{\mathrm{co}}|$ does not. Since we are assuming a Gaussian spatial profile, the filter function can be approximated by:

$$\mathcal{F}^{\mathrm{approx}}(\Omega) = \mathrm{erf}^2\left(\frac{\tilde{\Omega}L}{f\sigma_K}\right). \tag{59}$$

This is also plotted in Fig. 10 for $\sigma_K^{-1} = 100\ \mu$m, $L = 2.5$ cm, $f = 2.5$ cm and $d_o = d_i = 5$ cm. The effect of a collimating lens placed in the far field is therefore to limit the contribution to the profile of transverse wave vectors $|\boldsymbol{K}| < L\tilde{\Omega}/f$. The beam after collimation and focusing can be obtained by:

$$\boldsymbol{E}_+(\Omega, \boldsymbol{K}; d_o + d_i) = \boldsymbol{E}_+\left(\Omega, \boldsymbol{K}; d_o^-\right)\mathcal{F}^{\mathrm{approx}}(\Omega)e^{i\frac{2fK^2}{\tilde{\Omega}}}e^{iwd_i}. \tag{60}$$

The filter function $\mathcal{F}^{\mathrm{approx}}(\Omega)$ is for the finite size effect of the mirror, $e^{i\frac{2fK^2}{\tilde{\Omega}}}$ is the phase curvature introduced by an infinite lens with a focal length equivalent to that of the pair of matched mirrors, and e^{iwd_i} is a propagation factor from the lens to the focal plane. At $\Omega = 0$, the limit of Eq. (60) is zero. Experimental results of THz radiation that is collimated and refocused can be modelled very well with the combined use of near field expressions and filtering functions from collimating, focusing, and propagating the beam. For example, the calculation of THz radiation from optical rectification in a 30 μm ZnTe crystal detected in a 27 μm ZnTe crystal (similar to the experimental results reported by Han and Zhang[23]) is shown on Fig. 11. The calculation makes use of Eq. (50) with the additional multiplication by filter function Eq. (60). The detection *via* electro-optic sampling has been

described elsewhere[24] and is an additional filter function. The full dispersion curve of ZnTe is obtained from Leitenstorfer *et al.*[25] and is used in the calculation of the index of refraction $n_3(\Omega)$ at THz frequency, as well as for the electro-optic detection filter function. These calculations agree very well with published results[23]. The exact temporal profile is strongly dependent on the frequency-dependent index of ZnTe, and small temporal features are not easily reproduced when strong phonon resonances are present, as is the case here.

7. Conclusions

Plane waves with polarization basis $\hat{s}$ and $\hat{p}$ are ideal for describing the linear propagation of electromagnetic radiation, since these two polarizations can be treated independently even in the presence of layered structures. In an infinite medium, the Green function relating the radiated field to the source is known and the radiated electric field is obtained by integration over all plane waves of all frequencies and directions. In the far field, it is possible to simplify these integrals greatly, since only the plane waves having wave vectors in the direction of the observation point contribute to the field. In the near field, it is possible to simplify the expressions for the field if one makes the usual assumptions that are easily met in practice, such as linear polarization and Gaussian spatial profiles. The remaining integrals are then easily implemented numerically. The generality of the method and its applicability to *experimental situations* is demonstrated when thin film transfer matrices are used in conjunction with the boundary conditions (*i.e.*, incoming and outgoing waves) to obtain the Green function for a polarization embedded in a three-layer structure. This Green function is used to calculate the temporal profiles of the far and near field radiation for a spatially Gaussian polarization source (see Eqs (44) and (51)), and includes the dispersion of the source material, the multiple reflections in the material, and the polarization dependence of the transmissions and reflections at interfaces. Finally, a pair of mirrors,

often encountered experimentally to collimate and refocus a THz pulse, is shown to cut off low frequencies but to let through higher frequencies mostly unaltered. The cutoff frequency depends on the focal length, the size of the mirror, and the size of the THz source. A complete modelling of experiments is possible when the details of the frequency response of the THz detection system are known. The dispersive properties of various THz measurement schemes have been studied and compared elsewhere[8,24–26]. One example of experimental data from the literature[23] has been shown to be very well modeled by the formalism presented in this publication. The straightforward application to experimental situations of the model presented here allows one to extract details about the THz generation process, as has been demonstrated elsewhere by our group[14,27]. A computer implementation of the results for calculating the various THz temporal profiles presented in the present paper is available online[28].

8. Acknowledgements

We would like to thank F. Nastos and N. Laman for comments, as well as Photonics Research Ontario and the Natural Sciences and Engineering Research Council of Canada for financial support.

Appendix A: Angular expansion of the polarization tensors

The different Fourier decompositions $\sum_m \overleftrightarrow{f}_m \, e^{-im\phi}$ of the polarization tensors are calculated. For each frequency Ω and transverse wave vector $\boldsymbol{K}$, $\hat{s}$ and $\hat{p}_{i\pm}$ polarization vectors as well as $\hat{K}$ are defined in medium i as:

$$\hat{K} = \hat{x}\cos\phi + \hat{y}\sin\phi$$

$$\hat{s} = \hat{K} \times \hat{z} = -\hat{y}\cos\phi + \hat{x}\sin\phi$$

$$\hat{p}_{i\pm} = \frac{1}{\nu_i}\left(K\hat{z} \mp w_i\hat{K}\right) = \frac{K}{\nu_i}\hat{z} \mp \frac{w_i}{\nu_i}\hat{x}\cos\phi \mp \frac{w_i}{\nu_i}\hat{y}\sin\phi$$

1. *Non-vanishing* $\overleftrightarrow{f}_m(\hat{s}\hat{s})$

$$\begin{aligned}
\overleftrightarrow{f}_0(\hat{s}\hat{s}) &= \frac{1}{2}(\hat{x}\hat{x}+\hat{y}\hat{y}) \\
\overleftrightarrow{f}_{+2}(\hat{s}\hat{s}) &= \frac{1}{2}\left(-\frac{1}{2}(\hat{x}\hat{x}-\hat{y}\hat{y})\right)+\frac{i}{2}\left(-\frac{1}{2}(\hat{x}\hat{y}+\hat{y}\hat{x})\right) \\
\overleftrightarrow{f}_{-2}(\hat{s}\hat{s}) &= \frac{1}{2}\left(-\frac{1}{2}(\hat{x}\hat{x}-\hat{y}\hat{y})\right)-\frac{i}{2}\left(-\frac{1}{2}(\hat{x}\hat{y}+\hat{y}\hat{x})\right)
\end{aligned}$$

2. *Non-vanishing* $\overleftrightarrow{f}_m(\hat{p}_{\pm i}\hat{p}_{\pm j})$

$$\begin{aligned}
\overleftrightarrow{f}_0(\hat{p}_{\pm i}\hat{p}_{\pm j}) &= \frac{K^2}{\nu_i\nu_j}\hat{z}\hat{z}+\frac{w_iw_j}{2\nu_i\nu_j}(\hat{x}\hat{x}+\hat{y}\hat{y}) \\
\overleftrightarrow{f}_{+1}(\hat{p}_{\pm i}\hat{p}_{\pm j}) &= \mp\frac{1}{2}\left(\frac{Kw_j}{\nu_i\nu_j}\hat{z}\hat{x}+\frac{Kw_i}{\nu_i\nu_j}\hat{x}\hat{z}\right)\mp\frac{i}{2}\left(\frac{Kw_j}{\nu_i\nu_j}\hat{z}\hat{y}+\frac{Kw_i}{\nu_i\nu_j}\hat{y}\hat{z}\right) \\
\overleftrightarrow{f}_{+1}(\hat{p}_{\pm i}\hat{p}_{\pm j}) &= \mp\frac{1}{2}\left(\frac{Kw_j}{\nu_i\nu_j}\hat{z}\hat{x}+\frac{Kw_i}{\nu_i\nu_j}\hat{x}\hat{z}\right)\pm\frac{i}{2}\left(\frac{Kw_j}{\nu_i\nu_j}\hat{z}\hat{y}+\frac{Kw_i}{\nu_i\nu_j}\hat{y}\hat{z}\right) \\
\overleftrightarrow{f}_{+2}(\hat{p}_{\pm i}\hat{p}_{\pm j}) &= \frac{1}{2}\left(\frac{w_iw_j}{2\nu_i\nu_j}(\hat{x}\hat{x}-\hat{y}\hat{y})\right)+\frac{i}{2}\left(\frac{w_iw_j}{2\nu_i\nu_j}(\hat{x}\hat{y}+\hat{y}\hat{x})\right) \\
\overleftrightarrow{f}_{-2}(\hat{p}_{\pm i}\hat{p}_{\pm j}) &= \frac{1}{2}\left(\frac{w_iw_j}{2\nu_i\nu_j}(\hat{x}\hat{x}-\hat{y}\hat{y})\right)-\frac{i}{2}\left(\frac{w_iw_j}{2\nu_i\nu_j}(\hat{x}\hat{y}+\hat{y}\hat{x})\right)
\end{aligned}$$

3. *Non-vanishing* $\overleftrightarrow{f}_m(\hat{p}_{\pm i}\hat{p}_{\mp j})$

$$\begin{aligned}
\overleftrightarrow{f}_0(\hat{p}_{\pm i}\hat{p}_{\mp j}) &= \frac{K^2}{\nu_i\nu_j}\hat{z}\hat{z}-\frac{w_iw_j}{2\nu_i\nu_j}(\hat{x}\hat{x}+\hat{y}\hat{y}) \\
\overleftrightarrow{f}_{+1}(\hat{p}_{\pm i}\hat{p}_{\mp j}) &= \frac{1}{2}\left(\frac{Kw_j}{\nu_i\nu_j}\hat{z}\hat{x}\mp\frac{Kw_i}{\nu_i\nu_j}\hat{x}\hat{z}\right)+\frac{i}{2}\left(\frac{Kw_j}{\nu_i\nu_j}\hat{z}\hat{y}\mp\frac{Kw_i}{\nu_i\nu_j}\hat{y}\hat{z}\right) \\
\overleftrightarrow{f}_{-1}(\hat{p}_{\pm i}\hat{p}_{\mp j}) &= \frac{1}{2}\left(\frac{Kw_j}{\nu_i\nu_j}\hat{z}\hat{x}\mp\frac{Kw_i}{\nu_i\nu_j}\hat{x}\hat{z}\right)-\frac{i}{2}\left(\frac{Kw_j}{\nu_i\nu_j}\hat{z}\hat{y}\mp\frac{Kw_i}{\nu_i\nu_j}\hat{y}\hat{z}\right) \\
\overleftrightarrow{f}_{+2}(\hat{p}_{\pm i}\hat{p}_{\mp j}) &= \frac{1}{2}\left(-\frac{w_iw_j}{2\nu_i\nu_j}(\hat{x}\hat{x}-\hat{y}\hat{y})\right)+\frac{i}{2}\left(\frac{w_iw_j}{2\nu_i\nu_j}(\hat{x}\hat{y}+\hat{y}\hat{x})\right) \\
\overleftrightarrow{f}_{-2}(\hat{p}_{\pm i}\hat{p}_{\mp j}) &= \frac{1}{2}\left(-\frac{w_iw_j}{2\nu_i\nu_j}(\hat{x}\hat{x}-\hat{y}\hat{y})\right)-\frac{i}{2}\left(\frac{w_iw_j}{2\nu_i\nu_j}(\hat{x}\hat{y}+\hat{y}\hat{x})\right)
\end{aligned}$$

References

1. J. D. Jackson, *Classical Electrodynamics*, 2 ed. (John Wiley & Sons, New York, 1975), Chap. 9.

2. A. E. Siegman, *Lasers* (University Science Books, Mill Valley, Calif., 1986), Chap. 16.
3. R. Ell, U. Morgner, F. X. Kärtner, J. G. Fujimoto, E. P. Ippen, V. Scheuer, G. Angelow, T. Tschudi, M. J. Lederer, and A. B. B. Luther-Davies, Opt. Lett. **26**, 373 (2001).
4. C. Fattinger and D. Grischkowsky, Appl. Phys. Lett. **53**, 1480 (1988).
5. J. T. Darrow, X.-C. Zhang, and D. H. Auston, Appl. Phys. Lett. **58**, 25 (1991).
6. A. Bonvalet, M. Joffre, J. L. Martin, and A. Migus, Appl. Phys. Lett. **67**, 2907 (1995).
7. O. Dietrich, F. Krausz, and P. B. Corkum, Opt. Lett. **25**, 16 (2000).
8. S.-G. Park, M. R. Melloch, and A. M. Weiner, IEEE J. Quantum Electron. **35**, 810 (1999).
9. E. Budiharto, N.-W. Pu, S. Jeong, and J. Bokor, Opt. Lett. **23**, 213 (1998).
10. A. E. Kaplan, J. Opt. Soc. Am. B **15**, 951 (1998).
11. S. Feng, H. G. Winful, and R. W. Hellwarth, Opt. Lett. **23**, 385 (1998), errata issued in Optics Letters 23, p. 1141 (1998).
12. S. Hunsche, S. Feng, H. G. Winful, A. Leitenstorfer, M. C. Nuss, and E. P. Ippen, J. Opt. Soc. Am. A **16**, 2025 (1999).
13. S. Nekkanti, D. Sullivan, and D. S. Citrin, IEEE J. Quantum Electron. **37**, 1226 (2001).
14. D. Côté, N. Laman, and H. M. van Driel, Appl. Phys. Lett. **80**, 905 (2002).
15. J. E. Sipe, J. Opt. Soc. Am. B **4**, 481 (1987).
16. M. Born and E. Wolf, *Principles of Optics*, 6th ed. (Pergamon Press, New York, 1985), Chap. 1, p. 51.
17. A. E. Siegman, *Lasers* (University Science Books, California, 1986), Chap. 20.
18. J. D. Jackson, *Classical Electrodynamics*, 2 ed. (John Wiley & Sons, New York, 1975), Chap. 3, p. 131.
19. J. E. Sipe, Surf. Sci. **105**, 489 (1981).

20. A. Nahata, A. S. Weling, and T. F. Heinz, Appl. Phys. Lett. **69**, 2321 (1996).

21. *Handbook of Optical Constants of Solids*, edited by E. D. Palik (Academic Press, Orlando, 1985).

22. A. E. Siegman, *Lasers* (University Science Books, California, 1986), p. 637.

23. P. Y. Han and X.-C. Zhang, Appl. Phys. Lett. **73**, 3049 (1998).

24. G. Gallot and D. Grischkowsky, J. Opt. Soc. Am. B **16**, 1204 (1999).

25. A. Leitenstorfer, S. Hunsche, J. Shah, M. C. Nuss, and W. H. Knox, Appl. Phys. Lett. **74**, 1516 (1999).

26. H. J. Bakker, G. C. Cho, H. Kurz, Q. Wu, and X.-C. Zhang, J. Opt. Soc. Am. B **15**, 1795 (1998).

27. D. Côté, N. Laman, A. Springthorpe, and H. M. van Driel (unpublished).

28. A computer implementation of the calculations in C/C++ can be obtained at http://www.novajo.ca/thzcode.html.

List of Figure Captions

Fig. 1. Coordinate systems used in the calculations, sketched in the case where $\hat{s}$, $\hat{p}_\pm$ and $\boldsymbol{\nu}_\pm$ are real. a) Axial direction $\hat{z}$, wave vector component $\boldsymbol{K}$, and polarization $\hat{s}$. b) Polarization vectors $\hat{s}$ and $\hat{p}_\pm$ for plane wave directions $\hat{\nu}_\pm$. c) Vector decomposition of plane wave vector $\boldsymbol{\nu}_\pm$ into its transverse ($\boldsymbol{K}$) and axial ($\pm w\hat{z}$) components.

Fig. 2. Lens geometry used in calculation. The upward propagating beam is incident from $z < d_\circ$.

Fig. 3. Three layer geometry with polarization source in medium with index n_3.

Fig. 4. Temporal profile showing the far field at $z = 50$ mm for $2\pi\sigma_\Omega^{-1} = 200$ fs, $2\pi\sigma_K^{-1} = 1$ mm in a medium with $n_1^2 = 10 + i10^{-4}$, similar to dispersionless GaAs. The field follows the second time derivative of the polarization envelope function.

Fig. 5. Temporal profile showing the transition from near to far field for common THz parameters with $2\pi\sigma_\Omega^{-1} = 200$ fs, $2\pi\sigma_K^{-1} = 1$ mm in a medium with a dielectric constant $n_1^2 = 10 + i10^{-4}$ similar to dispersionless GaAs. Profile at top is at z = 0 mm, center is at z = 8 mm and bottom is at z = 50 mm. The arbitrary units are the same on all plots, and are the same as those used on Fig. 4.

Fig. 6. Temporal profile of THz radiation from below band gap optical rectification with $\sigma_\Omega/2\pi = 3.8$ THz at $z = 5$ cm. Inset: spectrum amplitude.

Fig. 7. Temporal profile of THz radiation from below band gap optical rectification with $\sigma_\Omega/2\pi = 1$ THz near and far from the source.

Fig. 8. Two lenses of focal lengths f' used to collimate and refocus a point source located at the focus of one of the lens are equivalent to a single lens with a focal length twice as short $f = f'/2$; d_o (d_i): distance between object (image) plane and lens.

Fig. 9. Diffraction of a Gaussian beam originating from $z = 0$, and transformation by a

lens at $z = d_o$. The field at $z = d_o + d_i$ is obtained. The inset shows how to estimate the cut-off frequency when the lens is far from a point source with $\tan\theta_{\rm co} = L/d_o \approx |\boldsymbol{K}_{\rm co}|/\tilde{\Omega}$.

Fig. 10. Magnitude of filter function $\mathcal{F}^{\rm full}$ (solid line) and $\mathcal{F}^{\rm approx}$ (dotted line) for $\sigma_K^{-1} = 100$ μm, $L = 2.5$ cm, $f = 2.5$ cm and $d_o = d_i = 5$ cm.

Fig. 11. Calculation of the temporal profile of THz radiation from below band gap optical rectification in a 27 μm thick ZnTe crystal detection in a 30 μm ZnTe crystal. These calculations agree very well with published results[23].

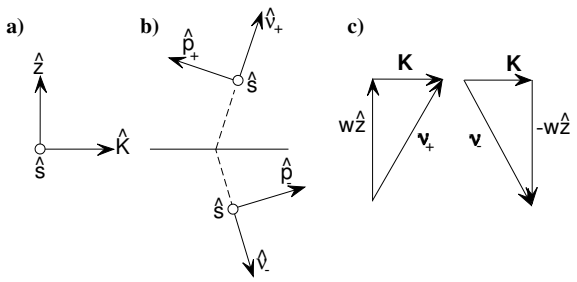

Fig. 1. Coordinate systems used in the calculations, sketched in the case where $\hat{s}$, $\hat{p}_\pm$ and $\boldsymbol{\nu}_\pm$ are real. a) Axial direction $\hat{z}$, wave vector component $\boldsymbol{K}$, and polarization $\hat{s}$. b) Polarization vectors $\hat{s}$ and $\hat{p}_\pm$ for plane wave directions $\hat{\nu}_\pm$. c) Vector decomposition of plane wave vector $\boldsymbol{\nu}_\pm$ into its transverse ($\boldsymbol{K}$) and axial ($\pm w\hat{z}$) components.

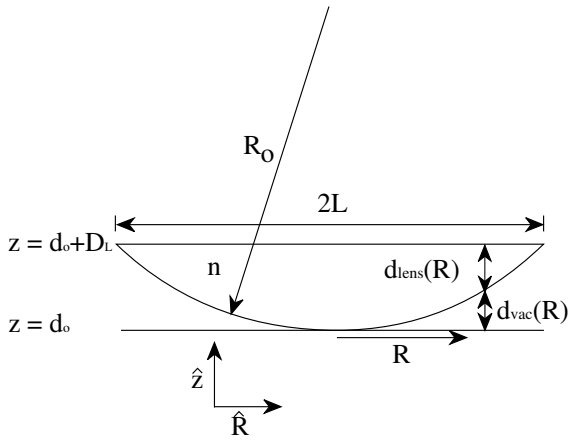

Fig. 2. Lens geometry used in calculation. The upward propagating beam is incident from $z < d_\circ$.

Fig. 3. Three layer geometry with polarization source in medium with index n_3.

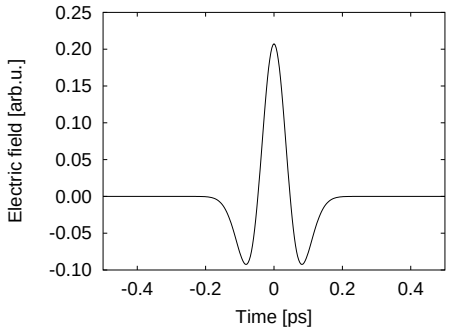

Fig. 4. Temporal profile showing the far field at $z = 50$ mm for $2\pi\sigma_\Omega^{-1} = 200$ fs, $2\pi\sigma_K^{-1} = 1$ mm in a medium with $n_1^2 = 10 + i10^{-4}$, similar to dispersionless GaAs. The field follows the second time derivative of the polarization envelope function.

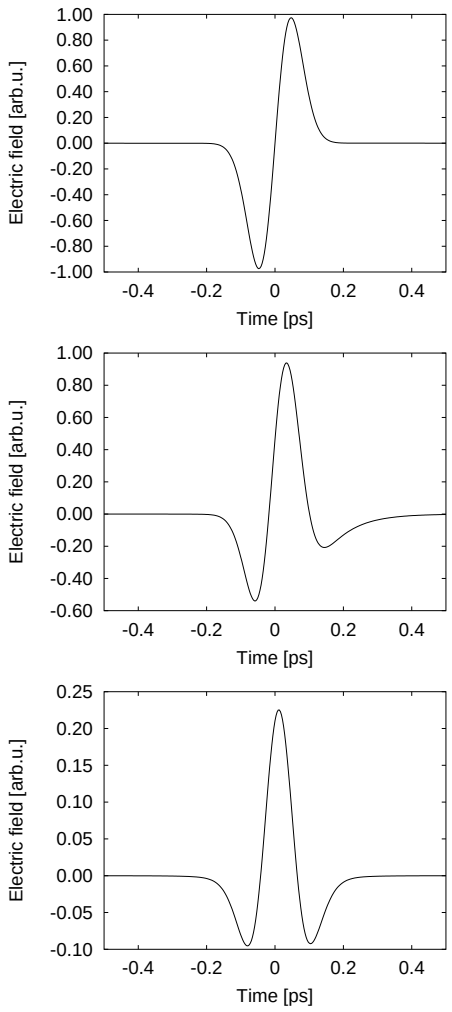

Fig. 5. Temporal profile showing the transition from near to far field for common THz parameters with $2\pi\sigma_{\Omega}^{-1} = 200$ fs, $2\pi\sigma_{K}^{-1} = 1$ mm in a medium with a dielectric constant $n_1^2 = 10 + i10^{-4}$ similar to dispersionless GaAs. Profile at top is at z = 0 mm, center is at z = 8 mm and bottom is at z = 50 mm. The arbitrary units are the same on all plots, and are the same as those used on Fig. 4.

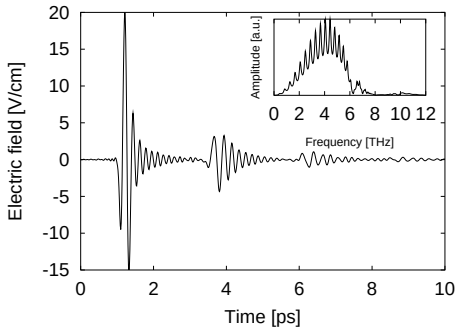

Fig. 6. Temporal profile of THz radiation from below band gap optical rectification with $\sigma_\Omega/2\pi = 3.8$ THz at $z = 5$ cm. Inset: spectrum amplitude.

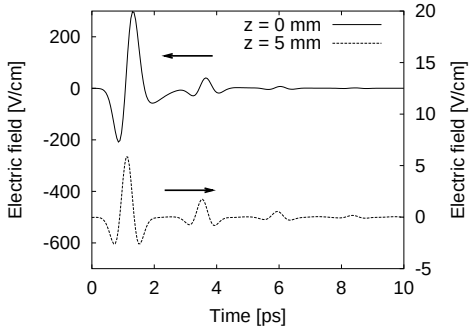

Fig. 7. Temporal profile of THz radiation from below band gap optical rectification with $\sigma_\Omega/2\pi$= 1 THz near and far from the source.

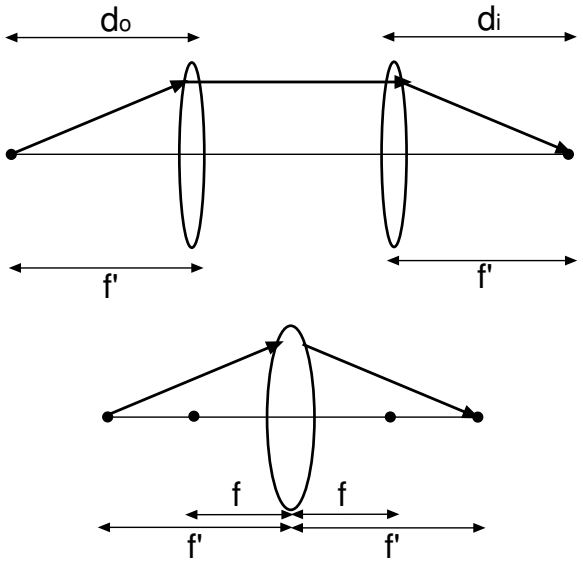

Fig. 8. Two lenses of focal lengths f' used to collimate and refocus a point source located at the focus of one of the lens are equivalent to a single lens with a focal length twice as short $f = f'/2$; d_o (d_i): distance between object (image) plane and lens.

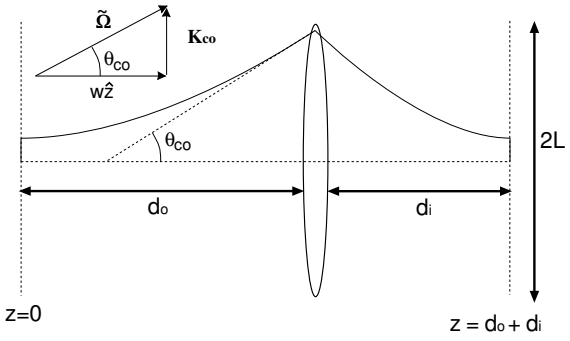

Fig. 9. Diffraction of a Gaussian beam originating from $z = 0$, and transformation by a lens at $z = d_o$. The field at $z = d_o + d_i$ is obtained. The inset shows how to estimate the cut-off frequency when the lens is far from a point source with $\tan\theta_{\rm co} = L/d_o \approx |\boldsymbol{K}_{\rm co}|/\tilde{\Omega}$.

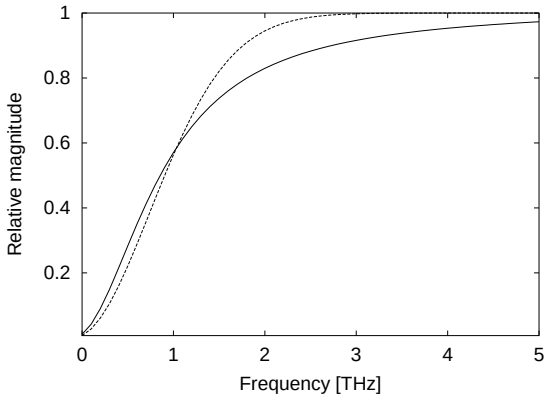

Fig. 10. Magnitude of filter function $\mathcal{F}^{\text{full}}$ (solid line) and $\mathcal{F}^{\text{approx}}$ (dotted line) for $\sigma_K^{-1} = 100$ μm, $L = 2.5$ cm, $f = 2.5$ cm and $d_o = d_i = 5$ cm.

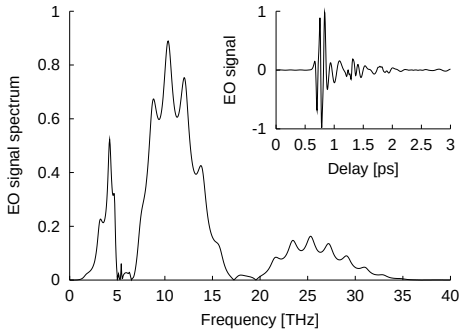

Fig. 11. Calculation of the temporal profile of THz radiation from below band gap optical rectification in a 27 μm thick ZnTe crystal detection in a 30 μm ZnTe crystal. These calculations agree very well with published results[23].